IAC–21–B4.5A

Modeling and Simulation of In-Orbit Centrifugal Casting of a Paraffin Wax Grain Inside a 3U CubeSat

Daniele Leuteri Costanzo
Space Systems Engineer, D-Orbit, Italy, daniele.leutericostanzo@dorbit.space

Keith Javier Stober
Research Engineer, Space Enabled Research Group, MIT Media Lab, stober@media.mit.edu

Danielle R. Wood
Assistant Professor; Director, Space Enabled Research Group, MIT Media Lab, drwood@media.mit.edu

Camilla Colombo
Associate Professor; Politecnico di Milano, Department of Aerospace Science and Technology, camilla.colombo@polimi.it

The work conducted by the authors, and described herein, investigates the possibility of performing centrifugal casting of paraffin into annular shapes while the spacecraft is orbiting the Earth. The adopted strategy involves the use, at the beginning-of-life, of the wax as a thermal insulator and, at the end-of-life, recast it as a fuel to allow a controlled re-entry of the satellite. The experiments currently conducted by the Space Enabled Research Group at 1g conditions have been characterized by the use of paraffin wax and beeswax as working fluids, with rotation rates ranging from 50-1500 rpm, and an initial temperature of 75-100 °C. All data relative to the paraffin wax has been derived experimentally by the Space Enabled Research Group. The polymer considered in this work has the formula of $C_{32}H_{66}$. The workflow is conceived such that the wax will be melted and conveyed into the combustion chamber, which will be spun by a DC motor, allowing the wax to be shaped into a hollow cylinder. Future extensions of this research effort will involve the design of a proper thermal bus capable of melting and conveying the wax inside the combustion chamber. This work is developed under the assumption that the wax is already inside the combustion chamber, and the simulations conducted take into account the grain formation phase and the re-entry trajectory design. The model developed to deliver the needed results is based on the propagation of a quasi-ISS orbit under the two-body problem assumption, including all relevant perturbations. The orbital dynamics is, then, coupled with the true attitude, measured by on-board sensors (a magnetometer and a Sun sensor are considered). At last, these two are coupled with a multi-node thermal model used for a transient thermal analysis, taking into account direct solar radiation, Earth albedo and infrared radiation, as well as internal power dissipation due to on-board electronics. It is shown that the stability of the spacecraft can be maintained with minimum effort, especially thanks to the low inertia of the rotating device. Also, with a passive thermal control based upon the use of a Multi Layer Insulator, the wax endures the eclipse-sunlight cycles and is kept below its melting temperature. The deorbit of the spacecraft can also be accomplished by considering the theoretical performances of the paraffin wax-based engine with one burn only, which is designed to lower the altitude of the spacecraft enough to induce atmospheric re-entry.[14]

keywords: space mission design, deorbit trajectory, paraffin wax, hybrid propulsion, thermal control, attitude control

1. Introduction

The main character of this research is paraffin wax, and this paper focuses on the development of a parametric simulation tool capable of simulating the centrifugal casting of a paraffin wax grain in microgravity. The covered aspects will be an overview on the overall mission design, with particular attention to the more critical aspects affecting the in-orbit centrifugal casting from an attitude stability point of view, as well as a proper thermal analysis that will drive the design of a passive thermal control. An example of a deorbit trajectory design, compliant with the theoretical capabilities of a paraffin wax based engine will be given as well. Since, in the first stage, the

paraffin will be used as thermal insulator, the reader will find in the current section a brief literature review on existing projects exploiting paraffin for this specific use case. More details about the whole experiment will be unveiled later on. The main classification for the thermal control is that it can be either active or passive. NASA, with its IceCube mission, exploited the use of paraffin wax in the form of Phase Change Material (PCM) packs to insulate some components, in order to meet the requirements in terms of operating temperature ranges.[5] In this framework, the paraffin is cast into small packs and they are attached near the components of interest, as in Figure 1; whereas, a detail of these 3 packs can be appreciated in Figure 2.

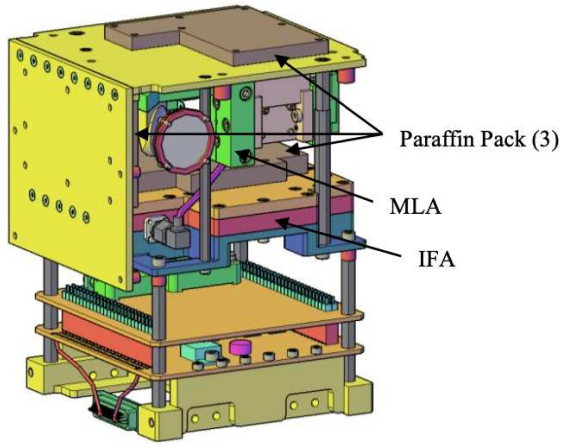

Fig. 1: Configuration with 3 mini-paraffin packs for the IceCube spacecraft[5]

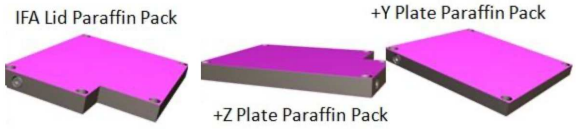

Fig. 2: Detail of the three mini-paraffin packs[5]

Therefore, the strategy is to use the paraffin to accumulate heat when the components are active and to dissipate it, through radiators, when they are switched off. During these operations, the phase of the paraffin varies, going from solid to liquid state (thus, the name *phase change materials*). This project is more ambitious, in the sense that the wax is meant to be used as propellant at the end of life, therefore a system capable of conveying the melted paraffin inside the combustion chamber shall be foreseen. The idea, then, is to melt the wax originally used as thermal insulator, with the purpose of using it as a thermal insulator, and convey it into the combustion chamber, which will spin at a certain rate, allowing the wax to be shaped into a caved cylinder, which is one of the most efficient shapes to burn the wax. For more details on the vision of Space Enabled Research Group,[1] the interested reader can find more details on their website. The aim of this work is to develop a parametric tool, with working environment set to be Matlab/Simulink, for the simulation of the thermal behavior of a spacecraft in Earth orbit, as well as performing mission analysis and thermal control design. Such tool shall be able to couple the orbital dynamics with the Attitude Determination and Control System (ADCS), and both with the thermal environment, in order to obtain the temperature profile of the paraffin wax unit and see how it behaves under the effect of the external environmental fluxes.

It is important to point out that while this work involves the implementation of all the aforementioned phases, it is assumed that the liquefied wax is already being transported inside the combustion chamber. Therefore, the design of the thermal bus that shall convey it from its initial form as PCM into the cylinder will not be part of this work. The simulation will take place, then, by considering the liquid wax just injected inside the combustion chamber, its rotation (in order to allow the formation of the grain) which lasts around 45 minutes, and then the focus will be mainly on the thermal control, in order to keep it below 75 °C.

2. Mission Design

2.1 Mission Modes

The main phases of the mission can be summarized in the following paragraphs, while their implementation will be covered throughout the paper.

2.1.1 Phase I - Deployment from the ISS

Being deployed directly from the ISS is common practice for many CubeSat missions nowadays, such as the LambdaSat-1, MicroMas-1, launched on 2014,[2] or the IceCube spacecraft, launched on 2015.[5] More informations on this device can be found in.[3]

The deployment takes place thanks to a device manufactured by the NanoRacks company, named

CubeSat Deployer. This device consists of a rectangular tube of anodised aluminum plates, base plate assembly, access panels and deployer doors, and its design allows a complete isolation - both mechanical and electronic - between the ISS and the CubeSat. The inside walls are designed so to minimize and/or preclude hang-up or jamming of the CubeSat appendages during deployment and to avoid unwanted contacts. Each NRCSD is capable of holding up to six CubeSat units, allowing it to launch 1U, 2U, 3U, 4U, 5U, and 6U (2×3 and 1×6) CubeSats. By using this device, the choice of the orbit is constrained, as it is imposed by the initial conditions at deployment. In particular, the resulting orbit will be characterised by 51.6 ° of inclination, and an altitude ranging between 400-415 km.[3] Therefore, the mission analysis design will be strongly limited.

2.1.2 Phase II - Detumbling

After being jettisoned by the deployer, the spacecraft will start to tumble, i.e. it spins without control about its axes; therefore, the first requirement is to bring it to the desired rotation rate. This will be accomplished by the ADCS subsystem, in particular - since the mission is meant to take place in a low orbit - it is possible to exploit the magnetic field and have magnetic torquers do the job.

2.1.3 Phase III - Launch and Early Orbit Phase

One of the most critical phases of the mission takes place. The Launch and Early Orbit phase (LEOP) consists in monitoring the satellite operations from its separation from the ISS up to the positioning on its final orbit. During this phase, there is a continuous monitoring from ground, in order to check that all the subsystems of the spacecraft (e.g. power systems, ADCS, telecom, etc.) are correctly operating; meanwhile, attitude correction maneuvers are performed.

2.1.4 Phase IV - Earth pointing / Science mode

During this phase the payload will be oriented towards Earth in order to take pictures; during this phase the most crucial target is to meet a high pointing accuracy.

2.1.5 Phase V - Grain formation

This is the most relevant phase for this mission. The paraffin, used as thermal coating in the first place, has to be melted and conveyed inside the combustion chamber. Once inside it, the liquid wax starts spinning and, in the meantime, it radiates heat in order to solidify again and to be later used as propellant for a controlled re-entry in Earth's atmosphere. This phase lasts about 45 minutes.

2.1.6 Phase VI - Deorbit

Once formed, the green propellant will be used to allow the spacecraft to deorbit and to shorten the reentry time. This phase is rather delicate, as - while the engine is firing - the stability of the spacecraft might be compromised, and so will the attitude.

2.1.7 Special modes

Other modes that will be taken into account and implemented in the mission profiles are the desaturation mode, so to allow reaction wheels' momentum dumping, and the Sun pointing mode, required in order to have batteries to be recharged.

Then, considering the different modes, each subsystem of the spacecraft can be described in terms of working condition. A summarising table is presented in Table 1.

2.2 Mission Analysis and Initial Conditions at Deployment

As explained in Subsection 2.1.1, the orbit is imposed by the deployer, and therefore the design of the orbit is strongly constrained. Hence, the only degree of freedom for this subsystem is represented only by the deorbit trajectory design, that will be covered later.

2.3 Initial conditions at deployment

NanoRacks manual do not contain informations about the initial conditions, in terms of angular velocities that the spacecraft will experience, therefore some random initial values were selected. However, the mechanism is made in such a way that the orbit injection will happen softly, and so the initial angular rates were chosen to be small; more of this will be covered in the detumbling results section.

3. Grain Formation

Among all of the mission modes, this is - for sure - the most important and peculiar one. Technically, this phase is composed of two parts: the first one is devoted in melting the wax and conveying it into the combustion chamber, the second is the one where the liquid wax is inside the cylinder and then - by means of an external DC brushed motor - it starts rotating in order to exploit centrifugal forces for distributing

the paraffin over the walls; once finished the process, it solidifies and the grain is ready to be used for the deorbit of the spacecraft.

MISSION MODE	TMTC	OBDH	ADCS	PAYLOAD	EPS	PS
Pre-deployment						
Deployment						
LEOP (Subsystems check)						
Detumbling						
Sunlit orbit						
Earth pointing						
Sun pointing						
Communication						
Eclipse						
Communication						
Special modes						
De-saturation						
Grain formation						
Disposal						

On	
Off	
Partially operational	

Table 1: Mission modes

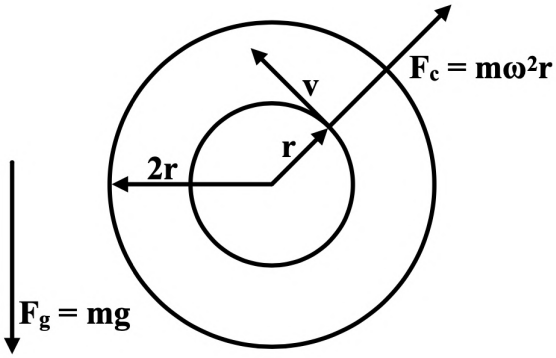

Fig. 3: Schematic representation of the problem[13]

At this point, the first part has not been engineered yet, and so this work assumes that the wax is already inside the combustion chamber and only the event related to the rotation is considered, in order to check - mainly that the stability of the spacecraft is preserved.

From previous investigations,[13] the adopted setup is the one in Figure 4.

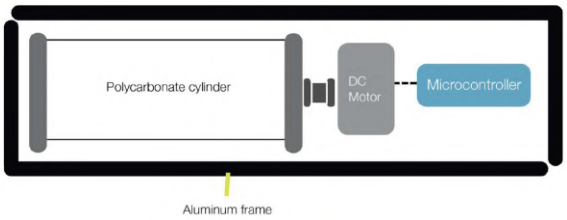

Fig. 4: Laboratory experiment setup[13]

The configuration has already been described, and taking into account the brushless motor, the whole apparatus is expected to occupy up to 1.5 U.

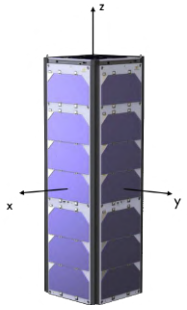

Fig. 5: Spacecraft body-fixed reference frame

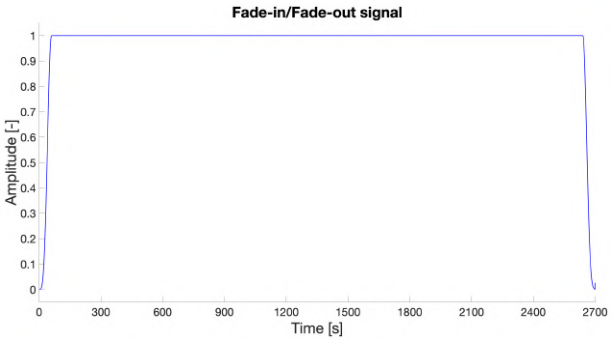

Fig. 6: Input signal - Grain formation

3.1 Attitude Control

In order to take this effect into account for the attitude stability, the overall spacecraft plus the internal rotational device has been modeled according to a dual spin spacecraft configuration; therefore, since the rotation acts along the z-axis (directed as in Figure 5), the dynamics of the spacecraft can be represented as:

$$\begin{cases} \dot{\omega}_x = \frac{I_y - I_z}{I_x}\omega_y\omega_z - \frac{I_r\omega_r\omega_y}{I_x} + \frac{d_x}{I_x} + \frac{u_x}{I_x} \\ \dot{\omega}_y = \frac{I_z - I_x}{I_y}\omega_x\omega_z + \frac{I_r\omega_r\omega_x}{I_y} + \frac{d_y}{I_y} + \frac{u_y}{I_y} \\ \dot{\omega}_z = \frac{I_x - I_y}{I_z}\omega_x\omega_y - I_r\omega_r + \frac{d_z}{I_z} + \frac{u_z}{I_z} \end{cases} \quad [1]$$

where I_x, I_y and I_y are the moments of inertia of the whole spacecraft, $\omega_x, \omega_y, \omega_z$ are the spacecraft's angular velocities expressed in the body frame, I_r and ω_r are the ones of the cylinder, while d_i and u_i are the disturbance and control torques, respectively.

By simple mass geometry equations, the inertia of the cylinder can be computed as:

$$I_r = \frac{M_r}{2}(r_i^2 + r_e^2) \quad [2]$$

giving a moment of inertia of $2.3 \cdot 10^{-3}\ kg \cdot m^2$, i.e. one order of magnitude smaller than the inertia moment of the spacecraft about the z-axis; this should hint that the attitude won't be strongly affected, given also the fact that - once it will spin at its maximum rate, which is expected to be 500 rpm, it should increase the gyroscopic stiffness.

To account for the DC motor, the input signal used to model its behavior is a fade-in fade-out signal, with symmetric windows for its rise and decay of about 300 ms (see Figure 6).

After that the unitary amplitude input signal is generated, it is - then - amplified by means of a gain block, in order to take into account the actual amplitude of the maximum rotational rate, plus a Gaussian white noise so to account for non-modeled disturbances that will arise in the real situation (e.g. sloshing effects).

3.1.1 Reduced Quaternion-Based Control Law

For the design of the control system, it has been decided to include a method based on the Linear Quadratic Regulator. This particular formulation has a structure that intervenes on the vector components of the quaternions.

This method turned out to be pretty helpful in the tuning of the feedback matrices **D** and **K**, that are expressed as a function of the cost matrices **Q** and **R**.

Such fine tuning has a twofold effect: it brings the system to converge in a reduced amount of time (with respect to non-optimal control techniques) and, incidentally, it reduces the power consumption.

Here, a brief description of the model will be given, but the reader will find all the details about the formulation in[16]

Let

$$\mathbf{J} = \begin{bmatrix} J_{11} & J_{12} & J_{13} \\ J_{21} & J_{22} & J_{23} \\ J_{31} & J_{32} & J_{33} \end{bmatrix} \quad [3]$$

be the inertia matrix of the spacecraft, assumed to be constant, and let

$$\omega = [\omega_1,\ \omega_2,\ \omega_3,]^T \quad [4]$$

be the angular velocity vector of the spacecraft. Moreover, let

$$\mathbf{u} = [u_1,\ u_2,\ u_3]^T \quad [5]$$

be the control torques. It is well-known that the spacecraft dynamics can be expressed by means of Euler equations as:

$$\mathbf{J}\dot{\omega} = -\omega \times \mathbf{J}\omega + \mathbf{u} \quad [6]$$

Now, let

$$q_0 = cos\left(\frac{\alpha}{2}\right),\ \bar{\mathbf{q}} = [\mathbf{q_1},\ \mathbf{q_2},\ \mathbf{q_3}]^T = sin\left(\frac{\alpha}{2}\right)$$

so that

$$\mathbf{q} = [q_0,\ \bar{\mathbf{q}}]^T \quad [7]$$

be the quaternion representating the rotation of the spacecraft in the body-fixed frame, with respect to the inertial (i.e. the quaternion corresponding to the attitude matrix $\mathbf{A_{BN}}$).

The nonlinear kinematics of the spacecraft can be represented, in terms of quaternions, as:

$$\begin{cases} \dot{\mathbf{q}} = -\frac{1}{2}\omega \times \mathbf{q} + \frac{1}{2}q_0\omega \\ \dot{q}_0 = -\frac{1}{2}\omega^T\mathbf{q} \end{cases} \quad [8]$$

Then, it can be shown that there exist a one-to-one mapping between $\dot{\mathbf{q}}$ and ω, such that:

$$\begin{bmatrix} \dot{\mathbf{q_1}} \\ \dot{\mathbf{q_2}} \\ \dot{\mathbf{q_3}} \end{bmatrix} = \frac{1}{2}\begin{bmatrix} f(q) & -q_3 & q_2 \\ q_3 & f(q) & -q_1 \\ -q_2 & q_1 & f(q) \end{bmatrix}\begin{bmatrix} \omega_1 \\ \omega_2 \\ \omega_3 \end{bmatrix} = \frac{1}{2}\Omega\omega \quad [9]$$

In this way, it is possible to write the linearized equations for the system dynamics by Taylor expansion of Equations 6 and 9 around an equilibrium point. Therefore, the system dynamics can be written in state-space form as follows:

$$\begin{bmatrix} \dot{\omega} \\ \dot{\mathbf{q}} \end{bmatrix} = \begin{bmatrix} 0_3 & 0_3 \\ \frac{1}{2}\mathbf{I}_3 & 0_3 \end{bmatrix}\begin{bmatrix} \omega \\ \mathbf{q} \end{bmatrix} + \begin{bmatrix} \mathbf{J}^{-1} \\ 0_3 \end{bmatrix}\mathbf{u} = \mathbf{A}\mathbf{x} + \mathbf{B}\mathbf{u} \quad [10]$$

where

$$\mathbf{A} = \begin{bmatrix} 0_3 & 0_3 \\ \frac{1}{2}\mathbf{I}_3 & 0_3 \end{bmatrix},\ \mathbf{x} = \begin{bmatrix} \omega \\ \mathbf{q} \end{bmatrix},\ \mathbf{B} = \begin{bmatrix} \mathbf{J}^{-1} \\ 0_3 \end{bmatrix} \quad [11]$$

This formulation gives, of course, a controllable system. Moreover, it can be shown that there exist diagonal matrices $\mathbf{D}$ and $\mathbf{K}$ such that the state feedback

$$\mathbf{u} = -[\mathbf{D}\ \mathbf{K}]\mathbf{x} = -\mathbf{G}\mathbf{x} \quad [12]$$

is the LQR design for the equations in 10. Indeed, as it will be show in the results section, the system achieves global stability thanks to this controller. Plus, it is well-known that this equation gives stability to the closed-loop system.

The goal of the LQR is to find optimal matrices D and K such that the control energy is minimized as well as optimizing the system performances.

For the linearised set of equations just described, the cost function to be minimised is:

$$L = \frac{1}{2}\int_0^\infty [\mathbf{x}^T\mathbf{Q}\mathbf{x} + \mathbf{u}^T\mathbf{R}\mathbf{u}]\ dt \quad [13]$$

where Q and R are positive definite matrices. The optimal control is given by:

$$\mathbf{u}(t) = -\mathbf{R}^{-1}\mathbf{B}^T\mathbf{F}\mathbf{x}(t) \quad [14]$$

where F is a constant positive definite matrix, solution of the algebraic Riccati equation:

$$-\mathbf{F}\mathbf{A} - \mathbf{A}^T\mathbf{F} + \mathbf{F}\mathbf{B}\mathbf{R}^{-1}\mathbf{B}^T\mathbf{F} - \mathbf{Q} = 0 \quad [15]$$

Since J is usually designed to be diagonal, from here on it'll be assumed that also Q and R will be diagonal (in any case, in engineering practice they're almost always assumed to be diagonal as well). Thanks to these assumptions, the problem can be simplified dramatically. Yang[16] shows that the Lyapunov function corresponding to such control law gives stability, as its time derivative is negative, complying with Lyapunov's second stability theorem. Therefore, it is possible to proceed with the design of the LQR and, deriving the expressions for the matrices D and K, yielding:

$$\mathbf{D} = diag\left(\sqrt{\frac{q_{1i}}{r_i} + J_{ii}\sqrt{\frac{q_{2i}}{r_i}}}\right) \quad [16]$$

and

$$\mathbf{K} = diag\left(\sqrt{\frac{q_{2i}}{r_i}}\right) \quad [17]$$

and so, Equation 14 becomes:

$$\begin{bmatrix}\dot{\omega}\\ \dot{\mathbf{q}}\end{bmatrix} = \begin{bmatrix} D_{11} & 0 & 0 & K_{11} & 0 & 0\\ 0 & D_{22} & 0 & 0 & K_{22} & 0\\ 0 & 0 & D_{33} & 0 & 0 & K_{33}\end{bmatrix}\begin{bmatrix}\omega\\ \mathbf{q}\end{bmatrix} \quad [18]$$

where

- $D_{11} = \sqrt{\frac{q_{11}}{r_1} + J_{11}\sqrt{\frac{q_{21}}{r_1}}}$
- $D_{22} = \sqrt{\frac{q_{12}}{r_2} + J_{22}\sqrt{\frac{q_{22}}{r_2}}}$
- $D_{33} = \sqrt{\frac{q_{13}}{r_3} + J_{33}\sqrt{\frac{q_{23}}{r_3}}}$
- $K_{11} = \sqrt{\frac{q_{21}}{r_1}}$
- $K_{22} = \sqrt{\frac{q_{22}}{r_2}}$
- $K_{33} = \sqrt{\frac{q_{23}}{r_3}}$

such that the closed-loop system can be written as:

$$\begin{bmatrix}\dot{\omega}\\ \dot{\mathbf{q}}\end{bmatrix} = \begin{Bmatrix} f(Q,R,J) & g(Q,R,J)\\ \frac{1}{2}\mathbf{I}_3 & \mathbf{0}_3\end{Bmatrix}\begin{bmatrix}\omega\\ \mathbf{q}\end{bmatrix} \quad [19]$$

In this way, by using the LQR design ensures that the spacecraft reaches the desired attitude, and so the stability, starting from any initial condition in terms of angular rates and orientation, in a short amount of time. In this way, when the spacecraft is close to stability, the linearised model gives its best at representing the actual nonlinear system.

3.1.2 Extended State Observer

Though the adopted control law for tracking a moving reference frame ensures asymptotic stability, it lacks in terms of uncertainties modeling.

As for the environmental disturbances, high fidelity models are available and have been thoroughly described in previous sections, but there are unexpected ones that aren't easy to predict, both in terms of their nature and magnitude. For such reason, an alternative control law - compatible with the fact that momentum exchange devices are being used - can be formulated as follows:[9]

$$\mathbf{u}_{id} = -k_1\omega + k_2\frac{\partial V(q_{e,4})}{\partial q_{e,4}}\cdot\mathbf{q}_e - \mathbf{d} \quad [20]$$

where the term $\mathbf{d}$ accounts for all the aforementioned disturbances.

However, even though there is no explicit model for uncertainties such as momentum wheel friction, higher order gravitational effects, sloshing, shifting center of mass and so on, it is possible to account for them by means of an *extended state observer*. The goal is to estimate all these uncertainties by introducing them into a disturbance torque term, and add it to the equations of motion. Hence, it is possible to rewrite the following equation:

$$\mathbf{J_0}\dot{\omega} = \mathbf{J_0}\omega\times\omega + \mathbf{u} + \mathbf{d}$$

as an extended state of the disturbance, by defining a vector variable ζ such that:

$$\begin{cases}\mathbf{J_0}\dot{\omega} = \mathbf{J_0}\omega\times\omega + \mathbf{u} + \mathbf{d}\\ \dot{\mathbf{d}} = \zeta\end{cases} \quad [21]$$

Therefore, an ESO can be defined as:

$$\begin{cases}\frac{d\hat{\omega}}{dt} = \mathbf{J_0^{-1}}(\mathbf{J_0}\hat{\omega}\times\hat{\omega} + \mathbf{u}) + \mathbf{J_0^{-1}}\hat{\mathbf{d}} + L_1(\omega - \hat{\omega})\\ \frac{d\hat{\mathbf{d}}}{dt} = L_2(\omega - \hat{\omega})\end{cases} \quad [22]$$

where the output is an estimated value of the disturbances, $\hat{\mathbf{d}}$. This value is then used to cancel the uncertainty using the applied torque with $\hat{\mathbf{d}}$. If the estimation is correct, the control will asymptotically converge to the desired state, otherwise it will be bounded to a region of the desired state. This type of control is known as *active disturbance rejection control*, and helps in improving the convergence rate and accuracy in the present of uncertain disturbance torques.

3.2 Results - Attitude Control

The results are quite good in terms of stability, and show that it is feasible - from the attitude point of view - to perform this operation. From Figure 7, the angular velocities show the effects of this spinning

device, corresponding to the beginning and the ending of this phase. In particular, at the beginning, for a moment, the angular velocity along z drifts away from the equilibrium condition, but then - thanks to the optimal quaternion-based controller - it is quickly recovered and the stability, for the whole duration of the phase (which is assumed to last for about 45 minutes), is granted. After the device stops spinning, a peak is shown in the same plot, and this is due to the fact that the momentum is exchanged back between the device itself and the spacecraft. However, again the controller - whose torques are shown in Figure 7, intervenes and re-establishes the stability.

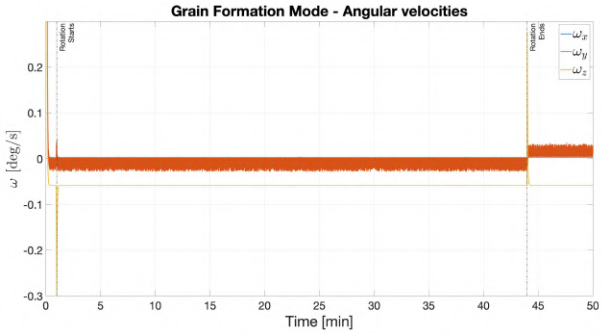

Fig. 7: Angular velocities - Grain formation

It was interesting to check also the pointing accuracy behavior during this phase. From Figure 8, it is possible to notice that this operation affects the pointing stability, indeed - even though it stays below 1°, it is still not suitable for picture acquisition; therefore, it should be better not to program picture acquisition while this mode is on.

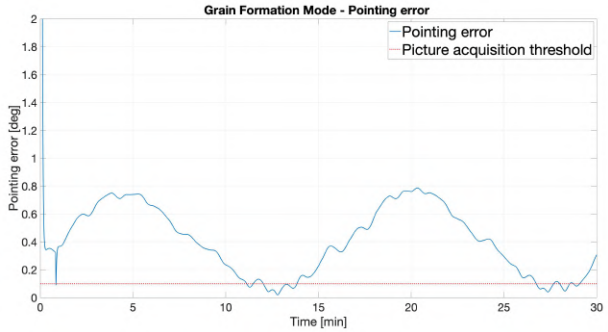

Fig. 8: Pointing error - Grain formation

In Figure 9 it is shown that the most stressed reaction wheel is the one acting along z. After this phase, a desaturation may be required. However, since the grain formation happens only at the end of life, there is no need to perform a momentum unloading, as the spacecraft will be injected into a graveyard orbit right away; this aspect will be further explained in the section concerning the deorbit trajectory design and optimisation.

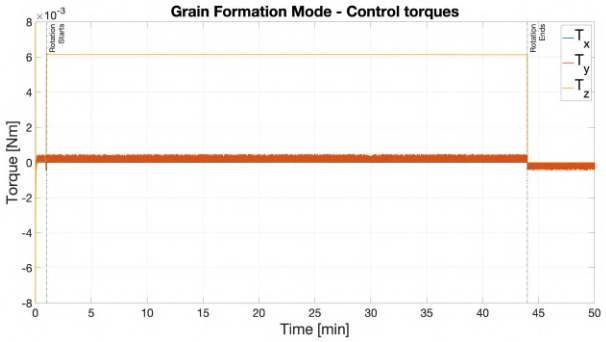

Fig. 9: Control torques - Grain formation

Hence, from the attitude point of view, these simulations confirm that the stability of the spacecraft won't be affected, as hinted already by the first "guess" considerations derived from comparing the inertia of the cylinder and the one of the spacecraft.

4. Thermal Environment Modelling

The thermal environment is what defines the boundary conditions at which the spacecraft is exposed. These are mainly determined by the orbital parameters, by the position of the Earth on the ecliptic, by external radiation sources (direct sunlight, Earth's albedo and infrared (IR) radiation).

Next, there will be a description of how these effects have been modeled and coupled with the orbital parameters and with the attitude.

4.1 Direct solar radiation

The first contribution taken into account is the radiation directly coming from the Sun. Such radiation is a function of the solar constant, $S_0 = 1322\ W/m^2$, which is basically the intensity of sunlight radiation, emitted at 1 AU (mean distance between Earth and Sun) and perpendicular to Earth's surface. Due to the fact that Earth's orbit around the sun is slightly elliptical, such value is not constant throughout the year; indeed, it ranges between $S_0 = 1322\ W/m^2$ at aphelion, to a maximum value of $S_0 = 1414\ W/m^2$ at perihelion, with a variation of $\pm 3.4\%\ W/m^2$

To model this effect and take into account the heat fluxes balance, one might model the incoming solar flux as:

$$Q_{s,i} = \alpha_i A_i cos(b_i) S_0 \quad [23]$$

where

$$cos(b_i) = \mathbf{n}_i \cdot \mathbf{s} \quad [24]$$

where $\mathbf{n}_i$ is the unit vector normal to the i-th surface of the satellite and $\mathbf{s}$ is the solar vector.
To proceed down this road, both vectors $\mathbf{n}_i$ and $\mathbf{s}$ must be expressed in the same frame of reference. In order to couple this analysis not only with the orbital position, it has been decided to express both vectors in the body fixed reference frame. In this way, the attitude, the orbit and the thermal environment are coupled with a high degree of accuracy.
Moreover, as already done with the solar radiation pressure model, also in this case the coupling affects this heat contribution: using the same shadow function, whenever the spacecraft is in Earth's shadow, $Q_s = 0\ W/m^2$, otherwise, it is computed as in Equation 23.

4.1.1 Reflected solar radiation

The solar radiation that hits the surface of the Earth and gets reflected is known as *albedo*. As we'll see with the infrared radiation, albedo varies across the globe, so depending on where we are located there will be a different value of reflected fraction of the incident solar flux. Therefore, in order to correctly account for it, one might adopt a model that takes into account the fact that the albedo coefficient, a, varies with latitude, longitude and time.

However, for sake of ease, it is assumed that the albedo coefficient is uniform around the globe; an averaged value is found to be $a = 0.273$.[8]

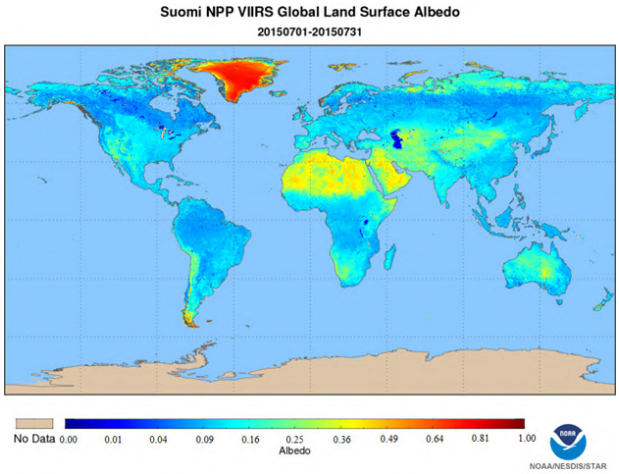

Fig. 10: Percentage of reflected solar flux,[4]

So, after dividing the surface of the Earth into patches (assumed to diffusely reflect equally in all the directions the incident radiation), it is possible to evaluate the infinitesimal contribution of a surface element, dS, as:

$$dQ_{A,i} = \alpha_i A_i a S_0 \frac{cos(a_E) cos(a_i) cos(b_E)}{\pi \rho^2} dS \quad [25]$$

and, integrating over the whole surface:

$$Q_{A,i} = \alpha_i A_i a S_0 F_{A,i} \quad [26]$$

where $F_{A,i}$ is the albedo view factor of the i-th surface of the spacecraft, evaluated as:

$$F_{A,i} = \int_S \frac{cos(a_E) cos(a_i) cos(b_E)}{\pi \rho^2} dS \quad [27]$$

In order to correctly evaluate this integral, all the vectors must be expressed in the same basis, and it is convenient to adopt a polar coordinate system.

However, for sake of ease, and to match the computational capabilities of the machine used to run these simulations, it is assumed that the view factors are the same as the ones evaluated for the infrared radiation. But, in this case, the dependence on the spacecraft position shall be considered, just like it has been done for the direct solar flux. So, the albedo heat has been included in the model and expressed as a function of the position of the spacecraft, similarly to what has been done with the solar radiation. Of course, also in this case, when the spacecraft is in Earth's shadow, this contribution goes to zero, as no light is reflected by the portion of Earth at which the satellite is exposed.

4.2 Infrared radiation

Both albedo and IR heat loads depend on radiation wavelength and other factors that bring uncertainties in the model (such as weather conditions).

If Earth is divided into a series of patches, each can be seen as a diffuse radiator, with radiosity I_E, defined as the flux leaving the patch per unit area. Such value isn't constant, indeed it depends on where the patch is located, meaning that there are regions on Earth with higher values for IR emission, and regions where this contribution is lower. Just like the albedo, so, we could write $I_E = I_E(\lambda, \phi, t)$, with λ and ϕ being the longitude and latitude, describing in a polar coordinate system the position of a point on Earth's surface. However, for sake of ease, the value of I_E is assumed to be constant; a widely adopted value for a time-averaged infrared heat flux is $I_E = 213\ W/m^2$, and this is the value that will be used throughout this work.

Therefore, by neglecting the dependence on the satellite position, it is possible to write the infinitesimal contribution to the heat flux, $dQ_{E,i}$ by considering the emission of an infinitesimal surface element of the globe, dS, as:

$$dQ_{E,i} = \epsilon_i A_i I_E \frac{cos(a_E)cos(a_i)}{\pi\rho^2} dS \qquad [28]$$

where:

- a_E is the angle between the normal to the patch element and the position vector of the spacecraft
- a_i is the angle between the position vector and the i-th normal of the surfaces of the spacecraft
- A_i and ϵ_i are the area and the emissivity of the i-th surface of the spacecraft
- ρ is the norm of the position vector of the spacecraft

integrating over all the surface elements:

$$Q_{E,i} = \epsilon_i A_i I_E F_{E,i} \qquad [29]$$

where we find that:

$$F_{E,i} = \int_S \frac{cos(a_E)cos(a_i)}{\pi\rho^2} dS \qquad [30]$$

is the radiative view factor, that can be evaluated by knowing the angles a_E and a_i, defined above.

In order to be correctly evaluated, this integral shall have all the terms written in the same reference frame, which has been chosen - again - to be the body fixed one; moreover, it can be convenient to write it in terms of appropriate polar coordinates.

Considering the attitude of the spacecraft described earlier, it can be shown that the view factor of the face -x yields:

$$F_{E,-x} = \frac{1}{h^2} \qquad [31]$$

whereas, for all the other surfaces:

$$F_{E,i} = -\frac{\sqrt{h^2-1}}{\pi h^2} + \frac{1}{\pi} \arctan\left(\frac{1}{\sqrt{h^2-1}}\right) \qquad [32]$$

The only face that has null view factor is the one in the $+x$ direction, as it never faces Earth (in this particular locked attitude condition).

5. Thermal control design

The thermal control system must ensure that the spacecraft components operate within their allowable temperature ranges, in particular during the worst conditions. Such conditions are derived by considering the worst hot and cold cases, which - in this study - are given by the sunlight and eclipse.

For such purpose, a transient thermal analysis, rather than a steady-state one, has been performed, in order to fully account for the orbital and attitude dynamics; ideally, given the starting Julian day, the position of the spacecraft is computed at each time step with respect to the position of the sun, switching the thermal and albedo fluxes for each position of the spacecraft orbiting the Earth and, incidentally, the Sun.

The main character of this thermal analysis is, for sure, the paraffin wax. As already mentioned, in this work it is assumed that the wax is already inside the combustion chamber, and so the thermal analysis is focused only in trying to keep the grain below its melting temperature.

5.1 In-orbit thermal environment

The environmental values for the incoming heat fluxes are described in Table 2, while the internal generated power is assumed to be $5W$, due mainly to on-board electronic components.

	Internal Power, W	**Solar flux,** W/m^2	**Albedo**	**Earth IR,** W/m^2
Max	5	1414	0.35	270
Min	5	1322	0.273	220

Table 2: Heat fluxes for worst cold and hot case

Considering the equations described earlier for the computation of the heat fluxes, a nominal condition yields the loads in Figure 11

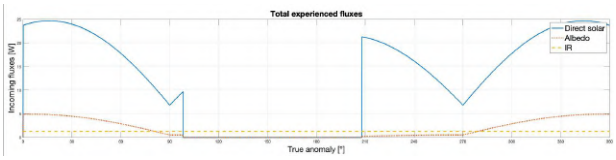

Fig. 11: Solar, albedo and IR fluxes

5.2 Passive thermal control design

In this stage of the mission, active thermal control methods are not needed; however, in the first part of the experiment, i.e. when the wax has to be melted, heaters might be sized, according to the strategy that the designer wants to adopt.

Assuming the structure of the spacecraft to be made of Aluminum 6061-T6, with body-mounted solar arrays, the optical properties are summarised in table 3

For sake of ease, these properties can be averaged over the full effective area of the spacecraft, following the guidelines from[7] and[15] in this way:

$$\alpha_{ave} = f_c \alpha_{eff} + (1 - f_c)\alpha_u \qquad [33]$$

where

- $f_c = 60.36\%$, as the area of a single cell is 30.18 cm^2,[12] and f_c represents the fraction of the face's area covered by solar cells (fig. 12)
- $\alpha_{eff} = \alpha_c - \eta$ is the effective cell absorbivity, function of the solar cells absorbivity, normally $\alpha_c = 0.91$ and of their efficiency; in this case, quad-junctions solar cells are considered,[12] whose efficiency $\eta = 0.32$
- $\alpha_u = 0.5$ is the absorbivity of the surface non covered by solar cells

yielding $\alpha_{ave} = 0.554$.

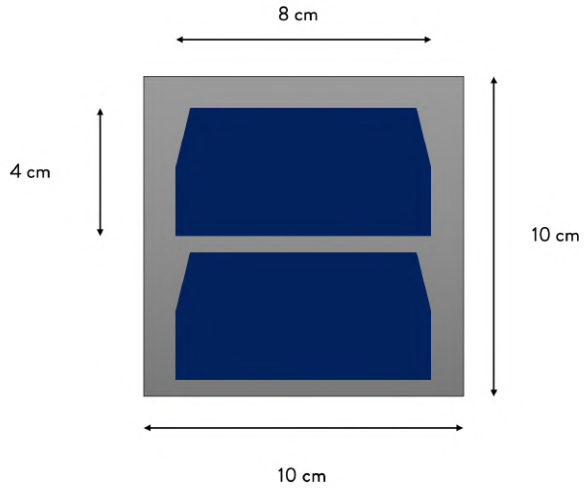

Fig. 12: Solar-cells covered face

The same can be done for the emissivity. Assuming $\epsilon_u = 0.05$, corresponding to a shiny metallic surface finish[8] for all the surfaces non covered by solar cells, an average value for the emissivity can be computed as:

$$\epsilon_{ave} = f_c \epsilon_c + (1 - f_c)\epsilon_u \qquad [34]$$

where $\epsilon_c = 0.89$,[12] and so $\epsilon_{ave} = 0.557$.

5.3 Paraffin wax temperature constraints

The temperature ranges are set between $0 - 70°C$; however, since the glass transition temperature of the paraffin wax is extremely low, the focus will be only into keeping it below $70°C$.

5.4 Thermal control of the paraffin wax engine

To have an idea of what could be a suitable surface finish for the insulation of the wax engine, a parametric analysis involving the optical properties of the materials, in terms of absorbivity and emissivity, has been performed.

Material	Emissivity, ϵ	Absorbivity, α	Density, kg/m^3	Thermal conductivity, W/mK	Heat capacity, J/kgK
Solar cells	0.85	0.90	5307	20	325
Aluminum 6061-T6	0.055	0.38	2700	201	900

Table 3: Spacecraft external optical properties

In this way, for a given temperature range, a set of values for α and ϵ have been evaluated. The temperature interval has been limited from 0 °C to 70 °C, as this is the range at which the paraffin wax can ideally work without melting.

Then, depending on the chosen orbital scenario, the tool will give back the plot in Figure 14

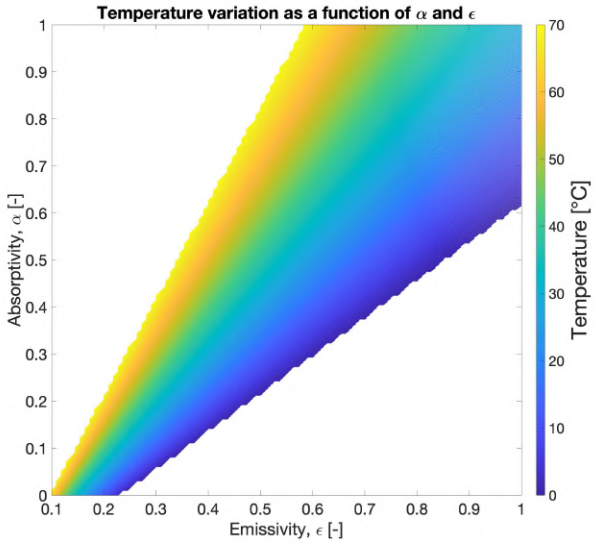

Fig. 14: Optical properties that grant the temperature to stay within the specified limits of 0 - 70 °C

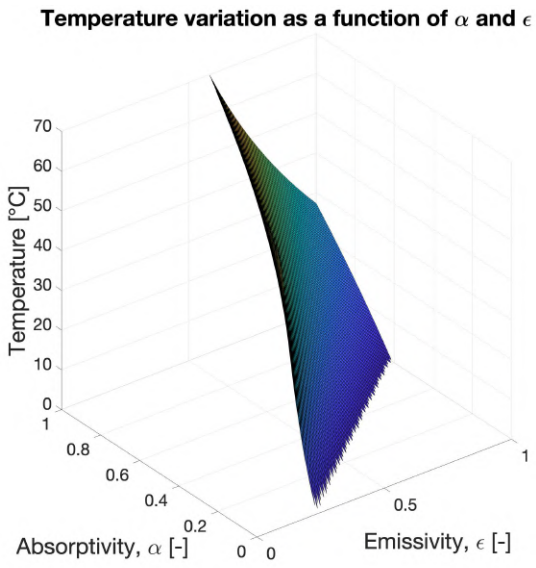

Fig. 13: Optical properties that grant the temperature to stay within the specified limits of 0 - 70 °C

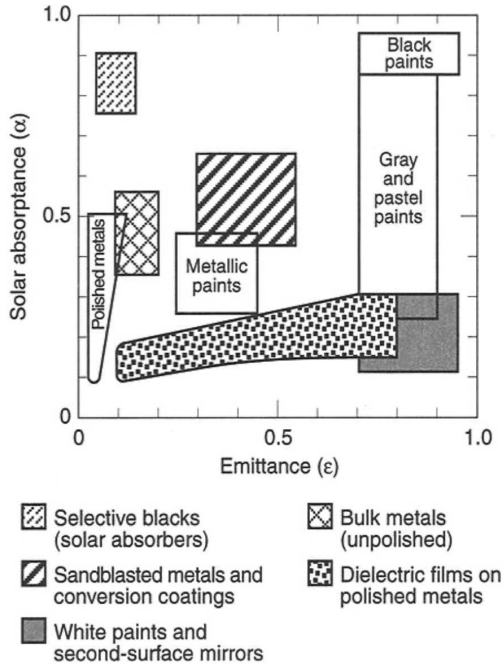

Fig. 15: Surface properties by type of finish,[8]

The parametric analysis hints the values of the optical properties that a material should have in order to keep it at temperatures near $60°C$, and this turns out to be pretty useful and precise, in terms of results, as it will be shown in a while. Then, by overlapping figure 14 with 15,[8] a sandblasted metal cover for the engine can be used.

5.5 Multi-node model design on Matlab/Simulink

The mathematical formulation for the energy equation in vacuum conditions (i.e. in space) can neglect the convective heat transfer, and may be represented as:

$$\rho C_p \frac{\partial T}{\partial t} = \nabla \cdot q_c^{''} - \nabla \cdot q_r^{''} + q^{'''} \quad [35]$$

where ρ is the density, C_p is the specific heat, T is the temperature. The first term on the right hand side of the equation, $\nabla \cdot q_c^{''}$ is the energy addition per unit volume by conduction, $\nabla \cdot q_r^{''}$ is the one due to radiation and the last term is the source term that accounts for internal heat dissipation (e.g. electronics, etc.).

At this point, based on the definition of conductive and radiative heat transfer given in the previous sections, based on a Thermal Network Approach, the final form of the energy equation can be represented as:

$$\frac{dT_i}{dt} \simeq \frac{1}{(mC_p)_i} \left[\sum_{j=1}^{N} C_{i,j}(T_i - T_j) + \sum_{j=1}^{N} R_{i,j}(T_j^4 - T_i^4) + q_i \right] \quad [36]$$

where $i = 1, 2, ..., N$ represents the number of nodes and m the correspondent mass; therefore, N is also the number of differential equations involved in the problem.

This set of ODE has been integrated by means of Matlab's *ode45*, with initial conditions set to $0°C$, whereas the number of nodes is set to 7: the six faces of the CubeSat, plus the wax-based engine.

Indeed, by considering black painting for the internal faces of the spacecraft and emissivity of $\epsilon = 0.6$ and an absorbivity $\alpha = 0.6$ for the coating of the paraffin wax cylinder unit, leading to a ratio $\alpha/\epsilon = 1$, the temperature of the wax unit settles to about $38°C$ and to about $42°C$ after 20 revolutions, in cold and hot cases respectively, with no huge differences to show (see Figure 16). Moreover, a simulation run considering a Sun synchronous orbit shows that - even in this hotter case - the coating is able to keep the wax under its melting temperature. Therefore, the chosen coating solution ensures that the temperature constraints are respected.

Such values of emissivity and absorbivity can be achieved by adopting a sandblasted metal surface finish, as mentioned earlier. For example, a Multi Layer Insulation (MLI) can be selected and modelled in order to have an outer cover with those values of emissivity and absorbivity. An optimal choice could be a combination of internal layers enclosed in a Vapour Deposited Aluminum (VDA) cavity, optimally tuned in order to achieve the desired values of α and ϵ.

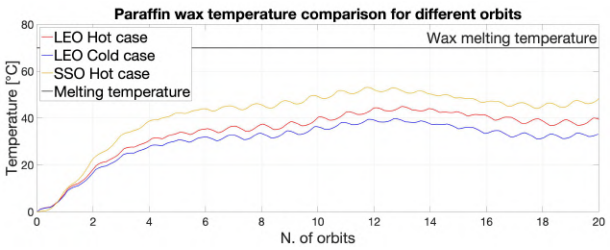

Fig. 16: Temperature evolution of the paraffin wax

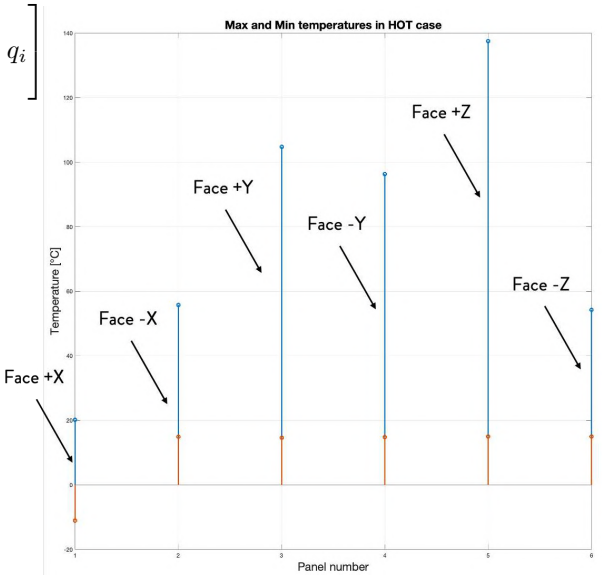

Fig. 17: Maximum and minimum temperature on the 6 faces of the spacecraft, hot case

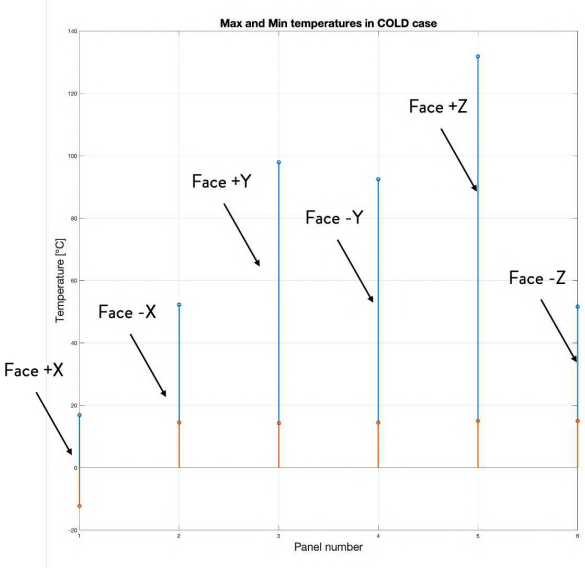

Fig. 18: Maximum and minimum temperature on the 6 faces of the spacecraft, cold case

As for the results, the differences between hot and cold cases are mainly related to the temperature of the faces of the spacecraft. Indeed, table 4 shows the differences in the computed temperatures among the 6 faces of the CubeSat. This analysis can be useful for later development and refinements in the configuration of the spacecraft itself (e.g. avoid a hot face for a component with lower temperature requirements, or vice versa). The stem plots in Figure 17 and in Figure 18 help in giving a better picture of the temperature conditions in the worst cases, considering the Earth at different positions on the ecliptic.

6. Deorbit Trajectory Design

The last part of this work involves the analysis of the performances related to the capabilities of a paraffin wax-based engine to deorbit a small satellite from a low Earth orbit.
As the design of the engine is not finalized yet, many assumptions were made and the results are inevitably affected; however, they still can be representative and perfectly suitable to give a hint on the real capabilities of the engine. Plus, some of the output results might serve as an input to the propulsion subsystem design, to have that work driven by the results coming from these simulations.

7. Design of the graveyard orbit

In this final section, the reader will go through the details of the deorbit trajectory design.

7.1 Equations of motion

A detailed analysis, in order to assess the real capabilities of an engine, cannot assume impulsive maneuvers. Therefore, it is necessary to take into account and model the equations of motion of the spacecraft under the assumption of non-impulsive maneuvers, as the thrust acts over a significant time interval. So, the equations of the two-body must account for the thrust;[6] namely, they read:

$$\ddot{\mathbf{r}} = -\frac{\mu}{r^3}\mathbf{r} + \frac{\mathbf{F}}{m} \qquad [37]$$

where $\mathbf{F}$ is an external force acting on the spacecraft and m is its mass.

In this case study, the external force acting on the spacecraft is the thrust given by the wax-based engine, yielding:

$$\mathbf{F} = T\frac{\mathbf{v}}{v} \qquad [38]$$

where T is the thrust and $\mathbf{v}$ is the velocity vector. Note that the sign of this force is positive when the force acts in the direction of the velocity vector, in this case, since it is needed to lower the orbit, the impulse must be given in the opposite direction, therefore in the equations of motion used to model this problem the sign is, then, minus. Substituting eq. 38 into eq. 37 leads to:

$$\ddot{\mathbf{r}} = -\frac{\mu}{r^3}\mathbf{r} + T\frac{\mathbf{v}}{v} \qquad [39]$$

where the Cartesian components are given by:

$$\begin{cases} \ddot{x} = -\mu\frac{x}{r^3} + \frac{T}{m}\frac{\dot{x}}{v} \\ \ddot{y} = -\mu\frac{y}{r^3} + \frac{T}{m}\frac{\dot{y}}{v} \\ \ddot{z} = -\mu\frac{z}{r^3} + \frac{T}{m}\frac{\dot{z}}{v} \end{cases} \qquad [40]$$

As the engine is firing, the spacecraft mass decreases, because propellant combustion products are being discharged through the nozzle. The mass decrease rate can be computed as:

$$\frac{dm}{dt} = -\frac{T}{I_{sp}g_0} \qquad [41]$$

where I_{sp} is the specific impulse and g_0 is the sea-level gravity acceleration.

Face	**+x**	**-x**	**+y**	**-y**	**+z**	**-z**
Hot case, $^\circ C$	6.4	40.2	95.8	88.9	123.6	42.9
Cold case, $^\circ C$	-28.6	-2.7	-2.5	-2.3	-0.7	0.2

Table 4: Spacecraft faces temperature in worst hot and cold cases

As no analytical solution can be sought for such complex system of equations, both 43 and 41 must be rewritten as a system of linear differential equations in the form:

$$\dot{\mathbf{y}} = \mathbf{f}(t, \mathbf{y})$$

Where the state vector $\mathbf{y}$ is, in this case, a 7x1 vector, made up by the position and velocity vectors, plus the mass. Therefore, we have:[6]

$$\mathbf{y} = \begin{Bmatrix} x \\ y \\ z \\ \dot{x} \\ \dot{y} \\ \dot{z} \\ m \end{Bmatrix}$$

its time derivative:

$$\dot{\mathbf{y}} = \begin{Bmatrix} \dot{x} \\ \dot{y} \\ \dot{z} \\ \ddot{x} \\ \ddot{y} \\ \ddot{z} \\ \dot{m} \end{Bmatrix}$$

and, finally:

$$\mathbf{f}(t, \mathbf{y}) = \begin{Bmatrix} y(4) \\ y(5) \\ y(6) \\ -\mu \frac{y(1)}{r^3} + \frac{T}{m} \frac{y(4)}{v} \\ -\mu \frac{y(2)}{r^3} + \frac{T}{m} \frac{y(5}{v} \\ -\mu \frac{y(3)}{r^3} + \frac{T}{m} \frac{y(6)}{v} \\ -\frac{T}{I_{sp} g_0} \end{Bmatrix} \quad [42]$$

Of course, these equations only take into account the external force due to the thrust, in terms of acceleration. For deorbiting problems, especially at low altitudes, there are two other factors to consider: the gravitational perturbation and the aerodynamic drag.The final equation of motion is the following:

$$\ddot{\mathbf{r}} = -\frac{\mu}{r^3}\mathbf{r} + \mathbf{p}_{J2} + \mathbf{p}_{drag} + \frac{\mathbf{T}}{m} \quad [43]$$

Then, the thrust is considered to be acting constantly and only during the burning time; this can be simply integrated by using the following logic:

$$\mathbf{T} = \begin{cases} eq.\ 38 & \text{if } t < t_{burn} \\ 0 & \text{if } t > t_{burn} \end{cases} \quad [44]$$

7.2 Engine parameters

At the time being, it is very difficult to find any work related to the design of a paraffin wax-based engine for CubeSats. Hence, its theoretical performances have been used to check their compliance with such a maneuver.

The main problem is related to the burning time: as[10] indicates, the works related to the design of hybrid engines - from various studies around the world - found clashing results on the burning time, ranging from 4.3 s up to a maximum of 80 s. But, again, these values are related to larger scale motors.

In this context, the burning time can be assumed to be derived by the following equation:

$$t_b = \frac{m_{prop}}{\dot{m}} \quad [45]$$

where m_{prop} is the propellant mass on-board the spacecraft, and $\dot{m}$ is the propellant mass flow rate, given by:

$$\dot{m} = \frac{T}{I_{sp} g_0} \quad [46]$$

Given a hypothetical input value of thrust equal to 70 N, and a specific impulse of 320 s, it is straightforward to derive a burning time of approximately 44.8 s, which falls in the range of the values indicated in,[10] and so it is a value that might be good for a first approximation. Moreover, from these data, it is also straightforward to derive - from Tsiolkovsky equation - the maximum theoretical deliverable ΔV, as:

$$\Delta V = I_{sp} g_0 ln\left(\frac{m_0}{m_f}\right) = 330\ m/s \quad [47]$$

Summarising the input data used to set up the problem:

- Thrust = 70 N
- I_{sp} = 320 s
- Burning time = 44.8 s
- ΔV_{max} = 330 m/s

As for the propellant mass, the scale of a 3U CubeSats sets some limitations in terms of maximum size and, incidentally, mass. As explained in the section related to the configuration of the spacecraft, the allowable space given to the engine is up to 1.5 U, therefore the grain will form accordingly to the already described geometry.

7.3 Ideal single impulse deorbit

An initial approach, to get a feeling of the order of magnitude of the results that should be expected, has been developed by following the algorithm described in,[11] where the ΔV required to deorbit a spacecraft from a generic circular Earth orbit is derived by means of the following equation. It basically assumes that a Hohmann transfer can be performed between an initial circular orbit and a final one, whose perigee falls within Earth's thicker layers of the atmosphere; for an illustration of the problem, see figure 19.

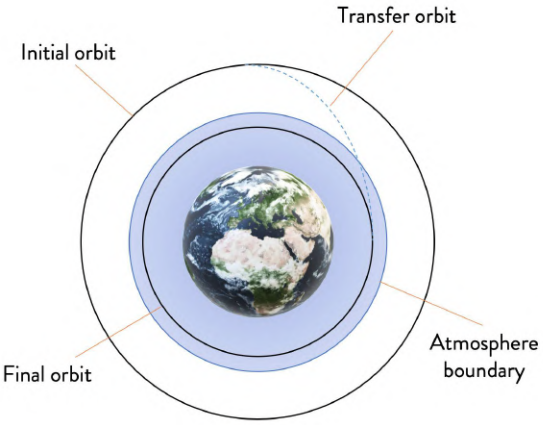

Fig. 19: Hohmann deorbit trajectory

$$\begin{aligned}\Delta V &= V_{Ce}\sqrt{\frac{1}{\bar{r}}}\left[1 - \sqrt{\frac{2(\bar{r}-1)}{\left(\frac{\bar{r}}{cos\gamma_e}\right)^2 - 1}}\right] \\ &= V_{Ci}\sqrt{\frac{1}{\bar{r}}}\left[1 - \sqrt{\frac{2(\bar{r}-1)}{\left(\frac{\bar{r}}{cos\gamma_e}\right)^2 - 1}}\right]\end{aligned} \quad [48]$$

where

- $\bar{r} = \frac{z_i + r_E}{z_e + r_E} = \frac{r_i}{r_e}$, orbit radius ratio
- $V_{Ce} = \sqrt{\frac{\mu}{r_e}}$, velocity of the circular orbit at the entry interface
- $V_{Ci} = \sqrt{\frac{\mu}{r_e}}$, velocity of the initial orbit
- γ_e, flight path angle at the entry interface
- z_i, altitude of the initial orbit
- z_e, altitude at the entry interface
- r_i, radius of the initial orbit
- r_e, radius at the entry interface
- r_E, Earth mean radius
- μ, Earth gravitational parameter

Then, to compute the true anomaly of the spacecraft at the entry interface, it is possible to use the following to equations:

$$sin\theta_e = \frac{\tilde{r}}{e_d}\sqrt{\frac{a_d(1-e_d^2)}{\mu}} \quad [49]$$

$$cos\theta_e = \frac{a_d(1-e_d^2)}{e_d r_e} - \frac{1}{e_d} \quad [50]$$

And extract the quadrant by using the inverse tangent operation:

$$\theta_e = tan^{-1}(sin\theta_e, cos\theta_e) \quad [51]$$

where

- e_d, eccentricity of the deorbit trajectory
- a_d, semi-major axis of the deorbit trajectory
- $\tilde{r} = -\sqrt{\frac{\mu\left[2a_d r_e - r_e^2 - a_d^2(1-e_d^2)\right]}{a_d r_e^2}}$

The time of flight between the maneuver point (i.e. apogee of the deorbit trajectory) and the entry interface can be easily derived by means of the time law,[6] yielding:

$$t(\theta_e) = \frac{\tau}{2\pi}\left[2tan^{-1}\left\{\frac{1-e_d}{1+e_d}tan\frac{\theta_e}{2}\right\} + -\frac{e_d\sqrt{1-e_d^2}sin\theta_e}{1+e_d cos\theta_e}\right] \quad [52]$$

where

- $\tau = \frac{2\pi}{\sqrt{\mu}}a_d^{1.5}$, orbital period of the deorbit trajectory

Hence, the time of flight between the maneuver point - assuming that it happens at the perigee of the initial orbit - and the entry interface is given by:

$$\Delta t = t(\theta_e) - t(\pi) - t(\theta_e) - \frac{\tau}{2} \quad [53]$$

Then, the velocity at the entry interface can be computed:

$$V_e = \sqrt{\frac{2\mu}{r_e} - \frac{\mu}{a_d}} \quad [54]$$

7.4 Optimisation strategy

Though the previous approach still leads to reasonable results and is quite helpful to get a feeling for the results, it should be clear that it does not take into account some crucial effects that, instead, must be considered. Therefore, the previous algorithm represents the fitness function that has been used inside the optimization algorithm.

The optimization algorithm is based on the equations of motion described in the previous section, and so on equation 43. In this way, the physical effects related to a non-impulsive maneuver is considered, because the equations of motion - as already explained - take into account the fact that the engine fires through a finite amount of time. Moreover, aerodynamic drag, Earth's J_2 effect and propellant consumption are as well included in the model, and such equations of motion are numerically integrated by means of Matlab's *ode45* function.

The objective function is set to be the scalar magnitude of the maneuver ΔV, while the constraints are imposed relatively to the flight path angle and the altitude at the entry interface. The control variables, instead, are represented by the true anomaly at the maneuver point, the ECI components of the maneuver ΔV and the time of flight. The initial guess for the Δ_V is given by equation 48, i.e. the ideal approach described earlier.

This calls for a *Nonlinear Programming Problem* (NPL), where the trajectory optimization problem can be described by the following dynamic system:

$$\mathbf{z} = \begin{bmatrix}\mathbf{y}(t)\\ \\ \mathbf{u}(t)\end{bmatrix}$$

where $\mathbf{y}(t)$ is the state variables vector and $\mathbf{u}(t)$ is the control variables vector. The state equations can be represented as follows:

$$\dot{\mathbf{y}} = \frac{d\mathbf{y}}{dt} = f[\mathbf{y}(t), \mathbf{u}(t), \mathbf{p}, t] \quad [55]$$

Where $\mathbf{p}$ is a vector of constant parameters, and the boundary conditions of the problem can be described by two dynamic variables, one defined for the initial time, t_0, and one for the final time, t_f, with state and control variables evaluated at these times.

Therefore, the aim is to minimise the scalar objective function:

$$J = \phi[\mathbf{y}(t_0), t_0, \mathbf{y}(t_f), t_f, \mathbf{p}] \mapsto min$$

In this way, the script numerically integrates eq. 43, while computing the errors in the target constraints, trying to drive them to zero. The two errors are computed by considering the difference between the computed value and the target one, with respect to the altitude and the flight path angle at the entry interface:

$$\epsilon_z = z - z_t$$

$$\epsilon_\gamma = \gamma - \gamma_t$$

Of course, the algorithm also requires upper and lower boundaries on the control variables. For such purpose, they have been chosen as:

- $180° \pm 10°$, for the true anomaly at the maneuver point, and also for the other control variables, symmetric conditions are chosen. In this case, the maneuver point should fall around the perigee of the initial orbit, which will turn into the apogee of the transfer orbit
- $\Delta V_{guess} \pm 15\%$, i.e. the lower and upper bounds are set to be between $\pm 15\%$ of the guess value of ΔV
- $TOF_{guess} \pm 30s$, for the time of flight between the maneuver point and the entry interface.

The optimization algorithm used is based on Matlab's *fmincon* and *gamultiobj*. The followed strategy was to give, as input to the genetic algorithm, the guess values computed with eqs. 48 - 53, using *gamultiobj* to sweep the solution space and then refine the results with *fmincon*.

8. Results

In this final section, the results of the trajectory optimization problem will be presented.

Before going into the details of the results, let us state the initial conditions that are common to both powered and non-powered re-entry trajectory. As already said, the initial orbit is a constraint of the mission, because it is imposed by the deployment mechanism attached to the ISS. Therefore, the initial orbital elements are given by:

The orbit in the ECI frame is represented in Figure 20, while its ground track after one cycle and one day is shown in figures 21 and 22 respectively.

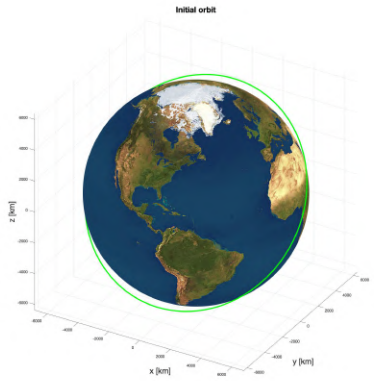

Fig. 20: Plot of the initial orbit

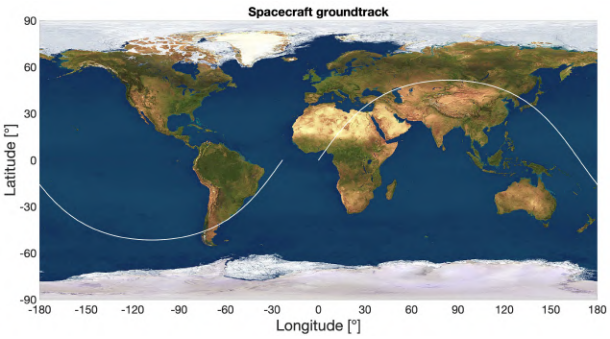

Fig. 21: Spacecraft ground track after 1 orbit

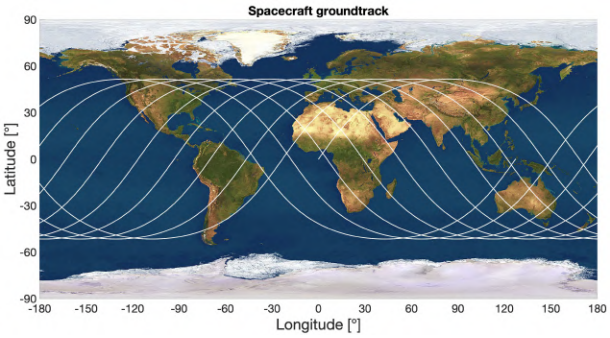

Fig. 22: Spacecraft ground track over 1 day

8.1 Powered re-entry

The input parameters used for the engine are the ones described in section 7.2, while - as for the control variables, the target flight path angle is set to -2° and the target altitude is set to 78 km, as it is assumed to be an optimal altitude for which a spacecraft burns into the atmosphere. The results for the ΔV optimization are summarised in table 6.

Orbital element	Value
Semi-major axis, km	6793
Eccentricity	0.0011
Inclination, deg	51.6
Right ascension of the ascending node, deg	0 (or user defined)
Argument of perigee, deg	0 (or user defined)
True anomaly, deg	0 (or user defined)

Table 5: Initial orbital elements

Method	ΔV, m/s	Time of flight, min
Guess value	144.19534	28.049
Genetic algorithm	185.87871	28.030
fmincon	182.39246	28.130

Table 6: Results, in terms of ΔV and TOF of the optimization

Note how the guess value of the ΔV is quite lower with respect to the results of the optimization process; this is exactly a reflection of what discussed earlier in terms of the approximations used for the computation of the ideal ΔV: the guess procedure does not take into account the full equations of motion of the spacecraft with all the disturbances, the optimization algorithm does. However, the results in terms of time of flight are quite similar and are way below the international guidelines threshold. This maneuver requires less than 1 kg of propellant.

8.2 Possible constraints on the propulsion subsystem design

As indicated in Section 7.2, the theoretical maximum ΔV is in the order of 330 m/s, and so it should be able to deorbit the spacecraft with one impulse. However, as the design of the engine isn't ready yet, it is possible to use these results as an input to the propulsion subsystem for the later stages of the design. For example, a driver to the design of the engine can be related to the burning time: with the burning time derived by considering the ratio between propellant mass flow rate and propellant mass computed according to the optimised trajectory, this kind of maneuver is perfectly achievable and allows the reenter of the spacecraft in about 30 minutes. But this should not be an issue; indeed, other simulations (see Table 7) with reduced burning time show a decrease in the needed ΔV to complete the maneuver, while leaving almost unchanged the time of flight between the maneuver point and the entry interface.

9. Conclusions

Despite the initial orbital conditions have been constrained by the assumptions of being released by the ISS, the developed tool is able to simulate any kind of Earth orbit and any kind of spacecraft, because each block that makes up the tool was built following a parametric approach. Therefore, the developed mission profiles implementation may be organised as needed, for future mission development.

This work gave also a first answer to the research objective, i.e. if it is possible to use a paraffin wax-based engine in order to deorbit a small satellite. It has been shown that it works and the re-entry times are absolutely reasonable and compliant with the international regulations. However, still no satellites have implemented this kind of propulsion system, and so this is just a feasibility analysis based on few assumptions on the real capabilities of the engine. For this reason, a lot of simplifying assumptions have been made, which strongly limited the work. However, the obtained results are still valid to prove that it is feasible to use a wax-based engine and, moreover, to cast it directly in microgravity.

This work, however, can't be representative of the full feasibility of the mission. Instead, it can be used as a basis to develop and refine all mission aspects covered throughout the paper, and - moreover - to implement new analysis and subsystems design. The latter is of the utmost importance, as a refined designed of the propulsion subsystem will help in defining the requirements for the other subsystems,

Method	ΔV, m/s	Time of flight, min
Guess value	144.19534	28.049
Genetic algorithm	160.99768	28.045
fmincon	79.55733	28.132

Table 7: ΔV optimisation with $t_{burn} = 10\ s$

such as the power generation, active thermal control for melting the wax, a thermal bus design - which is crucial for conveying the wax inside the combustion chamber. After defining all of these aspects, a more representative configuration can be characterised, and this will come in handy for a FE analysis on a commercial software.

This project has received funding from the European Research Council (ERC) under the European Union's Horizon 2020 research and innovation program (grant agreement No 679086 – COMPASS).

References

[1] *Candlewax Rockets: A green alternative for in-space propulsion.*

[2] *MicroMas-1 Mission.*

[3] *Nanoracks devices for CubeSats deployment.*

[4] *National Oceanic and Atmospheric Administration (NOAA).*

[5] Michael K Choi. Phase change material for maintaining temperature stability of icecube type of cubesats in leo. In *13th International Energy Conversion Engineering Conference*, page 3984, 2015.

[6] Howard D Curtis. *Orbital mechanics for engineering students*. Butterworth-Heinemann, 2013.

[7] Alejandro Garzón and Yovani A Villanueva. Thermal analysis of satellite libertad 2: A guide to cubesat temperature prediction. *Journal of Aerospace Technology and Management*, 10, 2018.

[8] David G Gilmore and Martin Donabedian. *Spacecraft thermal control handbook: cryogenics*, volume 2. AIAA, 2003.

[9] Biggs J.D. Spacecraft attitude dynamics and control course, A.Y. 2018-2019.

[10] Giuseppe Leccese, Enrico Cavallini, and Marco Pizzarelli. State of art and current challenges of the paraffin-based hybrid rocket technology. In *AIAA Propulsion and Energy 2019 Forum*, page 4010, 2019.

[11] AH Milstead. Technical notes deboost from circular orbits. *Journal of the Astronautical Sciences*, 13:170, 1966.

[12] AZUR SPACE. Solar power gmbh 0.32 quad junction gaas solar cells datasheet. 2019.

[13] Keith J Stober, Juliet Wanyiri, Alana Sanchez, Milo Hooper, Michael Mazumder, Suzanna Jiwani, Catherine Waft, Christine Joseph, Miles Lifson, and Danielle Wood. An investigation of the centrifugal casting of paraffin wax on earth and in microgravity. In *AIAA Propulsion and Energy 2019 Forum*, page 4012, 2019.

[14] Keith Javier Stober. *Optical investigation of hypergolic ignition and combustion in paraffin-based hybrid rockets*. PhD thesis, University of Stanford, 2017.

[15] James R Wertz. *Spacecraft attitude determination and control*, volume 73. Springer Science & Business Media, 2012.

[16] Yaguang Yang. Analytic lqr design for spacecraft control system based on quaternion model. *Journal of Aerospace Engineering*, 25(3):448–453, 2012.